Proceedings of the Fifteenth International Conference on
Computational Structures Technology
Edited by: P. Iványi, J. Kruis and B.H.V. Topping
Civil-Comp Conferences, Volume 9, Paper 10.6
Civil-Comp Press, Edinburgh, United Kingdom, 2024
ISSN: 2753-3239, doi: 10.4203/ccc.9.10.6

Numerical Modeling of 3D-Printed Alloy Structures

J. Vorel, A. Jíra and J. Kruis

Department of Mechanics, Faculty of Civil Engineering, Czech Technical University in Prague, Prague, Czechia

Abstract

The paper focuses on developing a complex numerical procedure for 3D-printed titanium alloys utilized for dental implants. An experimental campaign has been organized to study the influence of imperfections found in specimens that reach printing limits. The lower ultimate strength of thinner specimens is assigned to observed higher porosity. The specimens are printed from a powder that contains different-sized spherical particles. Therefore, the lattice discrete particle model, which can take the porosity into account, is used for numerical simulations. The theory of plasticity is utilized on facets defined in the model. Such a numerical tool is crucial for simulating the implant behaviour under different loading conditions and will allow/support a patient-specific design.

Keywords: lattice discrete particle model, 3D-printed material, porous structure, titanium alloy, plasticity, experimental data

1 Introduction

Biocompatibility and mechanical properties determine how an implant and human bone interact. Stress shielding plays a well-acknowledged role in the loss of bone mass, and excessive interface stresses between the implant and human bone can lead to

interface debonding and, ultimately, implant loosening. Using porous microstructures on the exterior of stiff implants as stabilising elements for relatively compliant human bone has garnered considerable attention, especially when considering the possibility of customising implants for each patient [1].

The production of suitable porous materials for bioengineering is challenging (Figure 1). However, the emergence of 3D printing technology in the past decade has revolutionised this field. It provides an efficient and effective means of creating these materials, including patient-specific implants. Furthermore, it enables the necessary surface treatment, a crucial factor in the successful osseointegration of the implant.

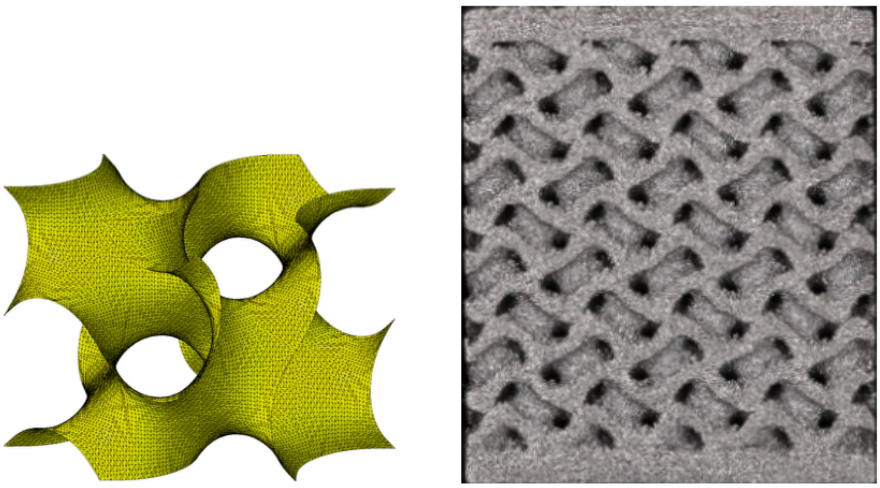

(a) (b)

Figure 1: Gyroid structure: (a) example of one-cell surface; (b) basic cells.

In the present paper, we focus our attention on the numerical modelling of 3D-printed alloy structures exhibiting flaws arising during production. People have been studying how solid materials behave for a very long time. Many theories, often based on the continuity of the displacement field, have been developed to describe and predict the mechanical or non-mechanical behaviour of solids. However, a class of models abandoning the displacement continuity assumption has also been formulated. Those models are typically composed of either basic structural elements that form a lattice network or discrete particles that tract at their mutual contact points [2]. The discrete models involve, e.g. classical lattice models, particle-based lattice models, and discrete element methods.

Our numerical study [3] and results presented in [4] show a relatively low stiffness of 3D-printed titanium specimens offered by experimental measurements compared to numerical predictions by order of magnitude. Such discrepancy is assigned to the flaws arising in the small-scale specimens during the 3D printing. Therefore, the main aim of this paper is to study the suitability of a numerical model based on the lattice

discrete particle model (LDPM) [5, 6] to study the behaviour of 3D-printed structures. More specifically, the influence of printing precision is of the main interest. LDPM can generate and simulate the material of interest at the particle scale to consider its size and distribution. The material behaviour is defined on the facets between adjacent particles [5].

2 Experimental data

The experimental campaign was focused on 3D-printed specimens for uniaxial tensile tests to obtain fundamental material characteristics specific to the 3D-printed titanium alloys. 3D-printed samples were created using the Selective Laser Melting (SLM) method, utilizing Ti25Nb4Ta8Sn or Ti6Al4V alloy powders. The powder size and distribution are documented in Figure 2. It can be seen that the average powder size is around 60 μm with a distribution from 20 to 140 μm.

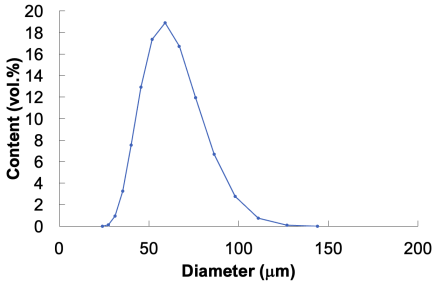

Figure 2: Size distribution of TiNbTaSn alloy powder used for SLM printing.

Mechanical testing in uniaxial tension was conducted using a LiTeM machine operating in controlled displacement mode. All dog bone specimens, schematically depicted in Figure 3, were vertically clamped within self-locking jaws and loaded along the longitudinal axis of the specimen. A loading rate of 0.04 mm/min was chosen following EN 10993 standards. The dog bone specimens with different thicknesses (500, 750, and 1000 μm) were produced to test the influence of flaws and, thus, printing quality. The experimental results for the Ti25Nb4Ta8Sn alloy with and without post-annealing are summarized in Table 1. As can be seen from the presented data, the influence of imperfections caused by the printing is more pronounced for the thinner specimens where the printer limits are reached, i.e., thinner specimens show higher porosity than the thicker specimens.

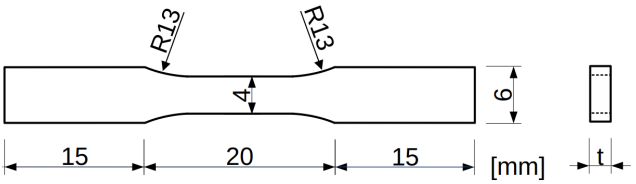

Figure 3: Geometry of dog bone specimens for uniaxial tensile tests with a thickness $t = 500, 750$ or $1000\,\mu$m.

t [μm]		units	with annealing	without annealing
500	$F_{\max}$	[N]	408 ± 12	208 ± 30
	$\sigma_{\max}$	[MPa]	204 ± 6	$135 \pm 15\ 5$
	E	[MPa]	3620 ± 108	37230 ± 410
750	$F_{\max}$	[N]	889 ± 38	674 ± 86
	$\sigma_{\max}$	[MPa]	296 ± 13	225 ± 29
	E	[MPa]	3810 ± 152	3970 ± 460
1000	$F_{\max}$	[N]	1443 ± 69	1011 ± 101
	$\sigma_{\max}$	[MPa]	361 ± 17	253 ± 25
	E	[MPa]	3940 ± 190	4184 ± 420

Table 1: Average values of ultimate force, ultimate tensile strength, and Young's modulus of elasticity for various thicknesses (Ti25Nb4Ta8Sn).

3 Lattice discrete particle model

In general, the lattice discrete particle model is often used to simulate the behaviour of quasi-brittle materials, such as rocks [7] and concrete [5], if the internal structure should be taken into account. The material is viewed as a group of stiff bodies (cells) interacting over the facets that are defined between them. These facets are considered to be between the neighbouring cells and can be thought of as possible crack surfaces. First, the volume under examination is filled with spherical particles. The lattice system that depicts the mesostructure topology is defined employing a Delaunay tetrahedralization of the particle centres and nodes used to characterize the external surface of the volume. Next, the system of polyhedral cells is designed according to the 3D tessellation. Note that many alternatives are used for the tessellation, as explained in [5] and [8], for example. Cells are formed by the aggregate and the matrix phase that surrounds the particles. Unlike the original LDPM formulation, in the current paper, the particle size distribution must be specified for the 3D-printed metals. The numerical model and incorporated flaws are shown in Figure 4.

Before proceeding to the detailed model description, stress and strain vectors defined on the facets are introduced. The rigid body kinetics is employed to describe the

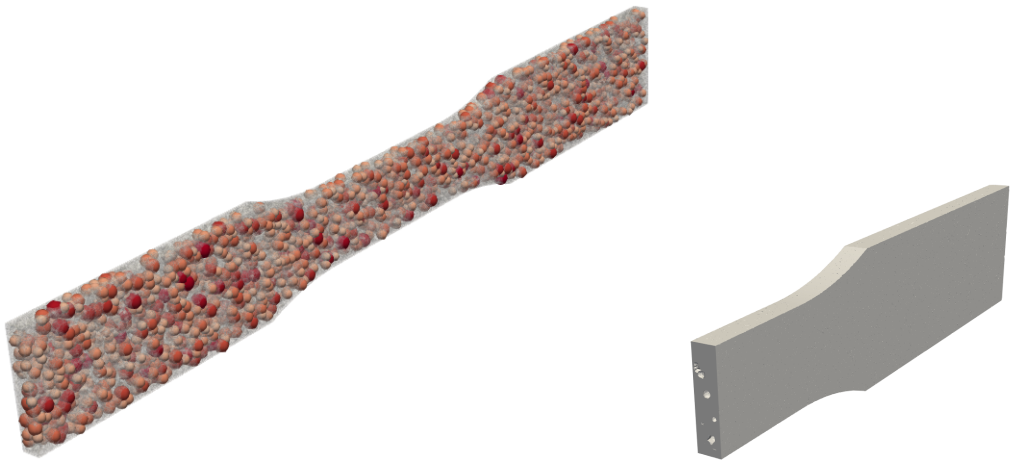

(a) (b)

Figure 4: LDPM model of dog bone specimen: (a) full model; (b) part of the model with flaws (voids) in the cross-section.

displacement vector, $\underline{u}$, associated with the facets [5]

$$\underline{u}\left(\underline{x}\right) = \underline{u}_i + \underline{\theta}_i \times \left(\underline{x} - \underline{x}_i\right), \tag{1}$$

where $\underline{u}_i$ and $\underline{\theta}_i$ are the translational and rotational degrees of freedom of node i with coordinate vector $\underline{x}_i$. For the given displacements and rotations of the associated particles, the relative displacement at the centroid of facet k can be determined as

$$\underline{u}_{Ck} = \underline{u}_{Cj} - \underline{u}_{Ci}, \tag{2}$$

where $\underline{u}_{Ci}$ and $\underline{u}_{Cj}$ are the displacements at the facet centroid caused by the translations and rotations of the adjacent nodes i and j, respectively. Displacement vector $\underline{u}_{Ck}$ is then employed to define the strain measures and discrete compatibility equations as follows

$$\varepsilon_{Nk} = \frac{\underline{n}_k{}^{\mathsf{T}}\underline{u}_{Ck}}{l_{ij}}, \quad \varepsilon_{Mk} = \frac{\underline{m}_k{}^{\mathsf{T}}\underline{u}_{Ck}}{l_{ij}}, \quad \varepsilon_{Lk} = \frac{\underline{l}_k{}^{\mathsf{T}}\underline{u}_{Ck}}{l_{ij}}, \tag{3}$$

where $\underline{n} = (\underline{x}_j - \underline{x}_i)/l_{ij}$, $\underline{m}$ and $\underline{l}$ are two mutually orthogonal vectors in the plane of the projected facet and $l_{ij} = \|\underline{x}_j - \underline{x}_i\| = [(\underline{x}_j - \underline{x}_i)^{\mathsf{T}}(\underline{x}_j - \underline{x}_i)]^{1/2}$. $\underline{x}_i$ and $\underline{x}_j$ stand for the positions of node i and j, respectively. It was pointed out in [9] that the aforementioned split into the normal and shear components is not able to recover the full Poisson ratio range ($-1 < \nu < 0.5$) and is limited to $\nu < 0.25$. Therefore, the volumetric-deviatoric split introduced in the Microplane models [10, 11] is considered. The volumetric-deviatoric split allows to recover the full Poisson ratio range needed for alloys. Because of the underlying tetrahedral mesh and corresponding facets Ω_e (see [5]) the volumetric (hydrostatic) strain is calculated as [12]

$$\varepsilon_{Vk} = \frac{1}{3\Omega_{e,0}} \sum_{k \in \mathcal{F}_e} \Gamma_k l_{ij} \varepsilon_{Nk}, \tag{4}$$

where $\Omega_{e,0}$ is the initial volume of the tetrahedral element, $\mathcal{F}_e$ is the set of facets belonging to one element and Γ_k and l_{ij} are the facet area and distance of the adjacent nodes corresponding to the facet, respectively. The normal deviatoric strain takes the form

$$\varepsilon_{NDk} = \varepsilon_{Nk} - \varepsilon_{Vk}. \tag{5}$$

Moreover, the shear (tangential) strain in the plane of the facet is written as $\varepsilon_{Tk} = (\varepsilon_{Mk}^2 + \varepsilon_{Lk}^2)^{1/2}$ and deviatoric strain as $\varepsilon_{Dk} = (\varepsilon_{NDk}^2 + \varepsilon_{Tk}^2)^{1/2}$. The corresponding stress components then read

$$\sigma_V = E_V \varepsilon_N, \quad \sigma_{ND} = E_D \varepsilon_{ND}, \quad \sigma_M = E_D \varepsilon_M, \quad \sigma_L = E_D \varepsilon_L, \tag{6}$$

where $E_V = E/(1-\nu)$ and $E_D = E/(1+\nu)$ are the volumetric and deviatoric moduli, respectively, related to Young's modulus E. The constitutive material law defined on the facets is described in the following section. By imposing the equilibrium through the principle of virtual work, the internal work and nodal forces associated with the facet can be calculated [5]. Note that subscript k is omitted in the following text for readability.

3.1 Material model

This section describes the material models used for the titanium alloys' plasticity. These models were inspired by the definition studied and described in [13] and are based on the volumetric-deviatoric split. More specifically, two lattice discrete particle models for plasticity, substantially different from each other, are discussed hereafter:

1) von Mises inspired material model,

2) equivalent stress based material model.

3.2 Von Mises inspired material model

In this material model, the yield condition is given similarly to the standard von Mises yield criterion (J_2 plasticity) in the form

$$f(\underline{\sigma}) = \sigma_{ND}^2 + \sigma_M^2 + \sigma_L^2 - \sigma_Y^2 = 0, \tag{7}$$

where σ_Y characterizes the magnitude of stress at yielding and is evaluated as $\sigma_Y(\kappa) = \sigma_0 + H\kappa$, where κ stands for the accumulated plastic strain, σ_0 is the initial yield stress, and H is the hardening modulus. When the condition in Equation (7) is satisfied, yielding occurs. The radial return is performed on the stress components σ_{ND}, σ_L and σ_M if $f(\underline{\sigma}) > 0$.

3.3 Equivalent stress based material model

The second model is defined by means of equivalent stress, σ^{eq}, and strain, $\varepsilon^{\mathsf{eq}}$. The equivalent strain has the form

$$\varepsilon^{\mathsf{eq}} = \sqrt{\left(\varepsilon_V + \alpha\varepsilon_{ND}\right)^2 + \alpha\left(\varepsilon_M^2 + \varepsilon_L^2\right)} = \sqrt{\left(\varepsilon_N^{\mathsf{eq}}\right)^2 + \alpha\varepsilon_T^2}, \tag{8}$$

where $\varepsilon_N^{\mathsf{eq}} = \varepsilon_V + \alpha\varepsilon_{ND}$, α stands for the interaction coefficient. This definition of equivalent normal strain originates from the assumption that $\sigma_N = E_V\varepsilon_N^{\mathsf{eq}}$. Based on the principle of virtual power, we relate the stress components to the equivalent stress as

$$\sigma_N = \sigma^{\mathsf{eq}}\frac{\varepsilon_N^{\mathsf{eq}}}{\varepsilon^{\mathsf{eq}}}, \quad \sigma_M = \sigma^{\mathsf{eq}}\frac{\alpha\varepsilon_M}{\varepsilon^{\mathsf{eq}}}, \quad \sigma_L = \sigma^{\mathsf{eq}}\frac{\alpha\varepsilon_L}{\varepsilon^{\mathsf{eq}}}, \tag{9}$$

and

$$\sigma_V = \sigma^{\mathsf{eq}}\frac{\varepsilon_V}{\varepsilon^{\mathsf{eq}}}, \quad \sigma_{ND} = \sigma^{\mathsf{eq}}\frac{\alpha\varepsilon_{ND}}{\varepsilon^{\mathsf{eq}}}. \tag{10}$$

By substituting Equations (9) and (10) into Equation (8), the effective stress is obtained in terms of normal and shear stresses

$$\sigma^{\mathsf{eq}} = \sqrt{\sigma_N^2 + \frac{\sigma_T^2}{\alpha}}, \quad \sigma_T = \sqrt{\sigma_M^2 + \sigma_L^2}. \tag{11}$$

If the elastic behaviour is assumed and taking into account Equations (9) and (10), the stresses are written as

$$\sigma_V = E^{\mathsf{eq}}\varepsilon_V, \quad \sigma_{ND} = \alpha E^{\mathsf{eq}}\varepsilon_{ND}, \quad \sigma_M = \alpha E^{\mathsf{eq}}\varepsilon_M, \quad \sigma_L = \alpha E^{\mathsf{eq}}\varepsilon_L, \tag{12}$$

where $E^{\mathsf{eq}} = \sigma^{\mathsf{eq}}/\varepsilon^{\mathsf{eq}} = E_V$ and thus $\alpha = E_D/E_V = 1 - 2\nu/1 + \nu$. This formulation covers the whole physical range of the Poisson ratio. In this model the yield condition is written as

$$f\left(\underline{\sigma}\right) = \left(\sigma^{\mathsf{eq}}\right)^2 - \sigma_Y^2 = 0. \tag{13}$$

When this condition is satisfied, yielding occurs. The radial return is performed on the equivalent stress if $f\left(\underline{\sigma}\right) > 0$.

4 Concluding remarks

The contribution gives an overview of the recently developed lattice discrete particle model for 3D-printed titanium alloys. The current numerical approach considers the intrinsic porosity caused by the printing procedure and utilizes the yield conditions for the model formulations associated with the facets. As presented in Table 1, the imperfections caused by the printing procedure significantly influence the specimen performance and are strongly pronounced for the smaller thicknesses close to the printing limits.

Acknowledgements

The financial support provided by the GAČR grant No. 23-04971S is gratefully acknowledged.

References

[1] C. Yan, L. Hao, A. Hussein, P. Young, Ti–6Al–4V triply periodic minimal surface structures for bone implants fabricated via selective laser melting, Journal of the mechanical behavior of biomedical materials 51 (2015) 61–73.

[2] J. Bolander, J. Eliáš, G. Cusatis, K. Nagai, Discrete mechanical models of concrete fracture, Engineering Fracture Mechanics 257 (2021) 108030.

[3] A. Jíra, M. Šejnoha, T. Krejčí, J. Vorel, L. Řehounek, G. Marseglia, Mechanical properties of porous structures for dental implants: experimental study and computational homogenization, Materials 14 (2021) 4592.

[4] H. Kolken, S. Callens, M. Leeflang, M. Mirzaali, A. Zadpoor, Merging strut-based and minimal surface meta-biomaterials: Decoupling surface area from mechanical properties, Additive Manufacturing 52 (2022) 102684.

[5] G. Cusatis, D. Pelessone, A. Mencarelli, Lattice discrete particle model (LDPM) for failure behavior of concrete. I: Theory, Cement and Concrete Composites 33 (2011) 881–890.

[6] G. Cusatis, A. Mencarelli, D. Pelessone, J. Baylot, Lattice discrete particle model (LDPM) for failure behavior of concrete. II: Calibration and validation, Cement and Concrete composites 33 (2011) 891–905.

[7] S. Ashari, G. Buscarnera, G. Cusatis, A lattice discrete particle model for pressure-dependent inelasticity in granular rocks, International Journal of Rock Mechanics and Mining Sciences 91 (2017) 49–58.

[8] J. Eliáš, Boundary layer effect on behavior of discrete models, Materials 10 (2017) 157.

[9] Z. Bažant, Y. Xiang, P. Prat, Microplane model for concrete. i: Stress-strain boundaries and finite strain, Journal of Engineering Mechanics 122 (1996) 245–254.

[10] I. Carol, Z. Bažant, Damage and plasticity in microplane theory, International Journal of Solids and Structures 34 (1997) 3807–3835.

[11] Z. Bažant, G. Zi, Microplane constitutive model for porous isotropic rocks, International journal for numerical and analytical methods in geomechanics 27 (2003) 25–47.

[12] G. Cusatis, R. Rezakhani, E. Schauffert, Discontinuous cell method (dcm) for the simulation of cohesive fracture and fragmentation of continuous media, Engineering Fracture Mechanics 170 (2017) 1–22. doi:https://doi.org/10.1016/j.engfracmech.2016.11.026.

[13] M. Brocca, Z. Bažant, Microplane constitutive model and metal plasticity, Applied Mechanics Reviews 53 (2000) 265–281.